3D-HGS: 3D Half-Gaussian Splatting

Haolin Li   **Jinyang Liu**   **Mario Sznaier**   **Octavia Camps**
Department of Electrical and Computer Engineering
Northeastern University
Boston, MA 02115
`{li.haolin,liu.jinyan}@northeastern.edu`
`{msznaier,camps}@ece.northeastern.edu`

Abstract

Photo-realistic 3D Reconstruction is a fundamental problem in 3D computer vision. This domain has seen considerable advancements owing to the advent of recent neural rendering techniques. These techniques predominantly aim to focus on learning volumetric representations of 3D scenes and refining these representations via loss functions derived from rendering. Among these, 3D Gaussian Splatting (3D-GS) has emerged as a significant method, surpassing Neural Radiance Fields (NeRFs). 3D-GS uses parameterized 3D Gaussians for modeling both spatial locations and color information, combined with a tile-based fast rendering technique. Despite its superior rendering performance and speed, the use of 3D Gaussian kernels has inherent limitations in accurately representing discontinuous functions, notably at edges and corners for shape discontinuities, and across varying textures for color discontinuities. To address this problem, we propose to employ 3D Half-Gaussian (**3D-HGS**) kernels, which can be used as a plug-and-play kernel. Our experiments demonstrate their capability to improve the performance of current 3D-GS related methods and achieve state-of-the-art rendering performance on various datasets without compromising rendering speed. The code and trained models are available at here.

1 Introduction

The pursuit of photo-realistic and real-time rendering of 3D scenes is a core focus in both academic and industrial sectors, with wide-ranging applications in virtual reality [10], media production [16], autonomous driving [25, 29], and extensive scene visualization [20, 12, 14]. Traditionally, meshes and point clouds have been the preferred methods for 3D scene representations due to their explicit compatibility with fast GPU/CUDA-based rasterization techniques. However, these methods often result in reconstructions of lower quality, plagued by various artifacts. In contrast, recent advancements in Neural Radiance Fields (NeRF) [15] have introduced continuous scene representations leveraging Multi-Layer Perceptron architectures (MLP). This approach optimizes novel-view synthesis through volumetric ray-marching techniques, providing significantly more realistic renderings. However, NeRF methods are characterized by their slow speed [4].

Recently, 3D Gaussian splatting (3D-GS) [8] has emerged as a state-of-the-art approach, outperforming existing methods in terms of both rendering quality and speed. The concept of using 3D Gaussians to parameterize a scene dates back to the early 2000s [32, 31]. This technique models a 3D scene with a collection of 3D Gaussian reconstruction kernels parameterized by 64 parameters. Initially, each Gaussian is derived from a point in a Structure from Motion (SfM) reconstruction. These parameters are subsequently refined through a dual process involving the minimization of image rendering loss and adaptive density adjustment. The efficiency of 3D-GS is enhanced by its GPU-optimized, tile-based rasterization method, enabling real-time rendering of complex 3D scenes.

Figure 1: **Qualitative comparison between 3D-GS and 3D-HGS.**

Employing 3D Gaussians as reconstruction kernels simplifies the volumetric rendering process and facilitates the integration of a low-pass filter within the kernel. This addition effectively mitigates aliasing during the resampling of scene data to screen space.

While 3D-GS takes the advantages of using a 3D Gaussian reconstruction kernel, it can be inefficient and lacks accuracy when modeling discontinuous functions which are common in 3D scenes on the edge of objects and texture-rich areas. To address this problem, we propose the use of 3D-Half-Gaussian Splatting (3D-HGS), which employs 3D-Half Gaussian as a novel reconstruction kernel. Characterized by a splitting plane, this kernel efficiently captures high-frequency information at discontinuities, while preserving the essential characteristics of the original 3D Gaussian kernel. This preservation is facilitated by the symmetric pairing of 3D Half-Gaussians, which can seamlessly represent the full 3D Gaussian. As a plug-and-play kernel, the proposed 3D-Half-Gaussian kernel preserves the key parameters in the original 3D-GS, providing the capability to be easily applied to existing 3D Gaussian kernel-based methods. Moreover, the learned normal of the splitting plane in the 3D Half-Gaussian also provides a solution to learning better surface normals in the 3D scenes. Our experiments show that using the proposed 3D Half-Gaussian as the reconstruction kernel achieved state-of-the-art rendering performance on MipNeRF-360, Tanks&Temples, and Deep Blending datasets.

Our main contributions are: (1) a new plug-and-play reconstruction kernel: the 3D Half-Gaussian, which can be used to improve the performance of 3D-GS existing methods without harming their rendering speed. (2) state-of-the-art reconstruction performance on various datasets with our proposed reconstruction kernel; our code will be available on our GitHub project page.

2   Related work

3D reconstruction and Novel View Synthesis (NVS) have long been pivotal goals within the field of computer vision. Notably, NeRFs have brought significant advancements in NVS, establishing a robust framework for synthesizing images from new viewpoints with unprecedented detail and realism. Recently, 3D-GS has emerged as a groundbreaking technique, setting new state-of-the-art (SOTA) benchmarks in this domain. In this section, we provide an overview of the historical and recent developments in 3D reconstruction and NVS, followed by a detailed analysis of 3D-GS, highlighting its methodologies, achievements, and impact on the field.

2.1   3D reconstruction and Novel View Synthesis

Before the advent of NeRFs, Multi-View Stereo (MVS) [18] and Structure from Motion (SfM) were commonly utilized for reconstructing 3D scenes from multiple viewpoint images. MVS relies on feature extraction from diverse images to correlate viewpoints and produce a final reconstruction, typically represented as a colored mesh grid or point cloud. However, due to its reliance solely on image features, achieving high-quality reconstructions can be challenging. SfM [17], employs multi-view images to generate a point cloud representing the 3D scene. In contrast to MVS, SfM excels in accurately estimating camera poses for different images, while MVS provides more precise 3D estimations of the architecture. Notably, SfM's simultaneous estimation of camera positions and point clouds makes it a preferred pre-processing step in recent advanced NSV methods.

NeRFs [15], stand as a significant milestone in NSV, demonstrating remarkable achievements in tasks such as image and view synthesis alongside scene reconstruction. Unlike previous methods, a Nerf represents the 3D architecture using a radiance field, treating the entire scene as a continuous function parameterized by position.

3D-GS [8], is a recently introduced NVS technique. This method boasts a remarkable reduction in both training and rendering times, surpassing the Nerf methods. Diverging from its predecessors, 3D-GS does not rely on training neural networks or any type of network architecture. Instead, it initiates from a point cloud and it employs spherical harmonics to depict the color for each Gaussian distribution. Unlike treating each point discretely, 3D-GS conceptualizes them as 3D Gaussian entities, each possessing a unique size and orientation. Subsequently, during the splatting stage, these 3D Gaussians are projected onto a 2D plane, with their appearances accumulated to generate renderings for a given viewing angle.

2.2 Splatting methods

The original concept of splatting was introduced by Westover [22, 23], and improved by Zwicker et. al [30, 32, 31]. Recently, the 3D-GS technique has achieved great success in photo-realistic neural rendering [8, 24].

Although 3D-GS has attained state-of-the-art performance in terms of rendering speed and quality, opportunities for further enhancements remain. Various studies [2, 3] have introduced modifications to the original 3D-GS framework. For instance, Mip-splatting [26] limits the frequency of the 3D representation to no more than half the maximum sampling frequency, as determined by the training images. Analytic-Splatting [11] employs a logistic function to approximate the Gaussian cumulative distribution function, thus refining each pixel's intensity response to minimize aliasing. Similarly, SA-GS [19] adapts a 2D low-pass filter during testing based on rendering resolution and camera distance. Scaffold-GS [13] employs voxel grids for initializing 3D scenes and utilizes Multi-Layer Perceptrons (MLPs) to constrain and learn voxel features. FreGS [27] introduces frequency-domain regularization to the rendered 2D images to enhance the recovery of high-frequency details. 2D-GS [7] aligns 3D scenes with 2D Gaussian kernels to improve surface normal representations. Lastly, GES [5] employs generalized exponential kernels to reduce the memory required to store 3D information.

The two papers most closely related to ours are 2D-GS [7] and GES [5], as they also focus on switching the reconstruction kernels. However, GES did not change the rasterizer but learned a scaling factor for each of the points to approximate different kernels. This method faces difficulties in complex 3D scenes. On the other hand, instead of doing a volumetric rendering as in the original 3D-GS, 2D-GS tries to do a surface rendering. Our method still learns a volumetric rendering of scenes to retain the rendering performance while enabling accurate modeling of discontinuous functions .

3 Methods

(a) The training and rendering pipeline for 3D half gaussian

(b) 3D Gaussian kernels
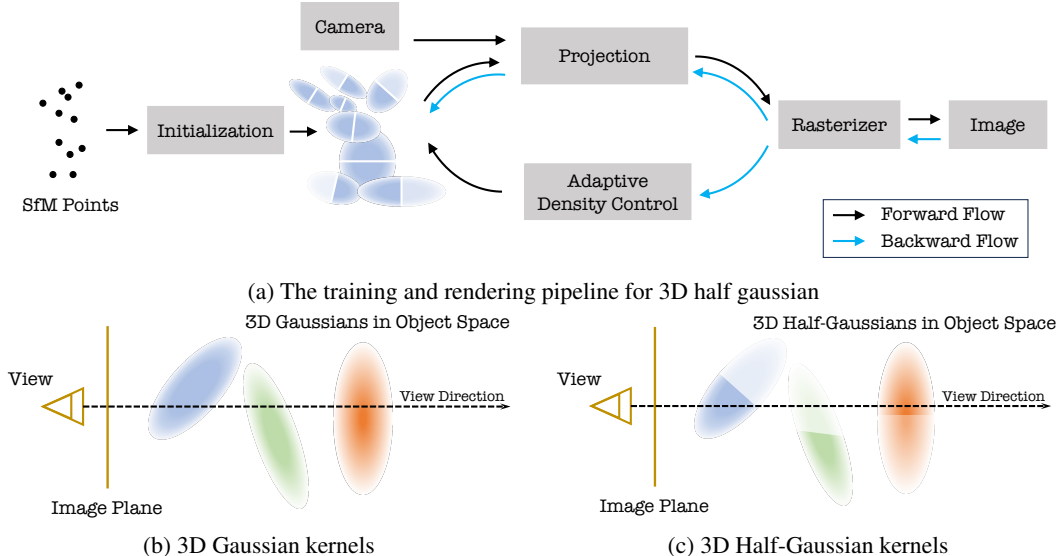
(c) 3D Half-Gaussian kernels

Figure 2: Illustration of the 3D-GS kernels and the proposed 3D Half-Gaussian kernels.

3D-GS [8] models the surface of 3D scenes using 3D Gaussian kernels [31, 32]. However, these kernels frequently encounter difficulties in accurately modeling 2D/3D discontinuous functions, which are prevalent in 3D scenes at edges, corners of objects, and texture-rich areas. The inefficiencies of the 3D Gaussian kernel in representing shape and color discontinuities can compromise the model's effectiveness. To overcome these limitations, we propose the use of a Half-Gaussian kernel for reconstruction. Section 3.1 provides an overview of the preliminary concepts related to 3D Gaussian Splatting, while Section 3.2 details our innovative approach to 3D Half-Gaussian splatting.

3.1 Preliminaries

3D-GS [8] represents the 3D scenes surface with parameterized antisotropic 3D Gaussian kernels [31, 32]. It starts from a sparse initial point cloud obtained using a Structure-from-Motion (SfM) step. Then, 3D Gaussians are mapped to 2D images through a GPU-specified tile-based rasterization. The parameters of these Gaussians are optimized, pruned, and added based on a loss function on the rendered images and ground-truth images.

Each of the 3D Gaussians is parameterized by their position (mean) μ, covariance-related scaling matrix, opacity α, and Spherical harmonics coefficients for color c. A 3D elliptical Gaussian $G_{\boldsymbol{\Sigma}}(\mathbf{x})$ centered at a point μ with covariance matrix $\boldsymbol{\Sigma}$ is given by:

$$G_{\boldsymbol{\Sigma}}(\mathbf{x} - \mu) = \frac{1}{(2\pi)^{3/2}|\boldsymbol{\Sigma}|^{\frac{1}{2}}} e^{-\frac{1}{2}(\mathbf{x}-\mu)^T \boldsymbol{\Sigma}^{-1}(\mathbf{x}-\mu)} \tag{1}$$

where $\mathbf{x}$ and μ are the column vectors $[x, y, z]^T$ and $[\mu_x, \mu_y, \mu_z]^T$, respectively, and $\boldsymbol{\Sigma}$ is a symmetric 3×3 matrix. The covariance $\boldsymbol{\Sigma}$ is further parameterized by a scaling matrix S and a rotation matrix R to maintain its positive semi-definite property:

$$\boldsymbol{\Sigma} = \boldsymbol{RSS}^T\boldsymbol{R}^T \tag{2}$$

As in the rendering function we will learn the opacity parameter α, we can merge the constant term $\frac{1}{(2\pi)^{3/2}|\boldsymbol{\Sigma}|^{\frac{1}{2}}}$ into α. Integrating a normalized 3D Gaussian along one coordinate axis results in a normalized 2D Gaussian. Thus, 3D Gaussians $G(x)$ can be efficiently transformed to 2D Gaussians $\hat{G}(\hat{x})$ on the image plane using a ray coordinate system representation [30]:

$$\int_{\mathbb{R}} G_{\boldsymbol{\Sigma}}(\mathbf{x} - \mu)dz = \hat{G}_{\hat{\boldsymbol{\Sigma}}}(\hat{\mathbf{x}} - \hat{\mu}) \tag{3}$$

where $\hat{\mathbf{x}} = [x, y]^T$ and the mean and covariance $\hat{\mu} = [\mu_x, \mu_y]^T$ and $\hat{\boldsymbol{\Sigma}}$ can be easily obtained by taking the top-left 2×2 sub-matrix of $\boldsymbol{\Sigma}$:

$$\boldsymbol{\Sigma} = \begin{pmatrix} a & b & c \\ b & d & e \\ e & d & f \end{pmatrix} \Leftrightarrow \begin{pmatrix} a & b \\ b & d \end{pmatrix} = \hat{\boldsymbol{\Sigma}} \tag{4}$$

Finally, the pixel values on the 2D image are obtained by α-blending:

$$C(\hat{\boldsymbol{x}}) = \sum_{i \in \mathcal{N}} c_i \alpha_i \prod_{j=1}^{i-1} (i - \sigma_j), \alpha_i = \alpha_i \hat{G}(\hat{\boldsymbol{x}}) \tag{5}$$

where $\hat{x}$ is the queried pixel position and $\mathcal{N}$ is the set of sorted 2D Gaussians associated with $\hat{x}$.

3.2 3D Half-Gaussian

In this section we provide a detailed description of the proposed method. We begin by giving the definition of the half Gaussian kernel and how to parameterize it, followed by how to project it to 2D and use it for rendering.

We propose to use 3D Half-Gauusians, where each half can have different opacity values α_1 and α_2. The half Gaussians are obtained by splitting a 3D Gaussian into two halves with a plane through its center. Note that this representation includes as a special case the 3D-GS representation in the case when $\alpha_1 = \alpha_2$. However, incorporating a planar surface into the kernel allows to represent sharp changes, such as edge and textures, as well as planar surfaces, more accurately. Furthermore, as seen below, the increase in the required number of parameters needed is very modest: the normal of the splitting plane and an additional opacity term, while the increase in computational cost reduces to a multiplication by a scaling factor.

A 3D Half-Gaussian is described by:

$$HG_{\boldsymbol{\Sigma}}(\mathbf{x}) = \begin{cases} e^{-\frac{1}{2}(\mathbf{x}-\boldsymbol{\mu})^T \boldsymbol{\Sigma}^{-1}(\mathbf{x}-\boldsymbol{\mu})} & \mathbf{n}^T(\mathbf{x} - \mu) \geq 0 \\ 0 & \mathbf{n}^T(\mathbf{x} - \mu) < 0 \end{cases} \tag{6}$$

5

(a) 3D Gaussian kernels　　　　　(b) Mapping the Half-Gaussian to image plane in the ray space
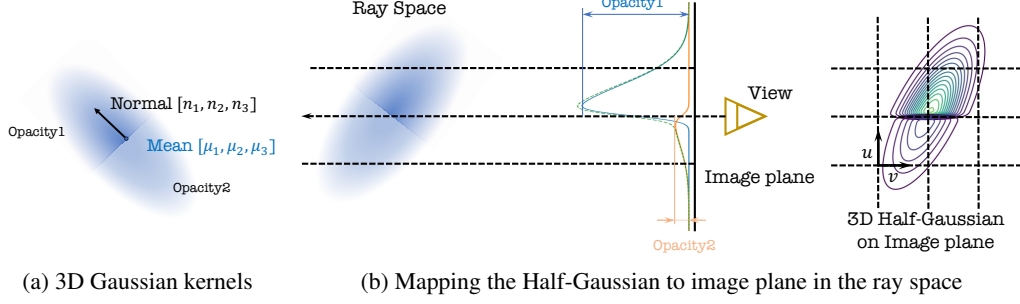
Figure 3: Illustration of the 3D-HG kernel, and the mapping of 3D Half-Gaussian to a 2D image.

where $\mathbf{n} = [n_1, n_2, n_3]^T$ is the normal of the splitting plane, represented as a column vector, while the other half Gaussian is obtained by changing the sign of the normal. The integration of a 3D Half Gaussian along the z axis yields a similar result as Eq. 3, except for a scaling factor related to the normal of the splitting plane:

$$\int_{\mathbf{n}^T(\mathbf{x}-\mu)\geq 0} HG_{\mathbf{\Sigma}}(\mathbf{x} - \mu)dz = \left(1 + \mathrm{erf}\left(\frac{n_1 x + n_2 y}{\sqrt{2}n_3}\right)\right)\hat{G}_{\hat{\mathbf{\Sigma}}}(\hat{\mathbf{x}} - \hat{\mu}) \tag{7}$$

Eq. 7 gives a closed-form solution for calculating the integration of 3D Half-Gaussian. The right-hand side of Eq. 7 consists of two factors: $(1 + \mathrm{erf}(\frac{n_1 x + n_2 y}{\sqrt{2}n_3}))$ is a scaling factor related to the normal of the splitting plane, while $\hat{\mathbf{x}} - \hat{\mu}$ is the same as in the original 3D Gaussian in Eq. 3.

For rasterization, we follow a similar process as in 3D-GS, except that we use the proposed 3D Half-Gaussian as the reconstruction kernel. For enhanced parameter efficiency, we represent pairs of Half-Gaussians, since the parameters for mean, rotation, scaling, and color are shared between the two halves of a Gaussian, while we learn the orientation of the splitting plane and two opacity parameters, one for each side of the splitting plane. Thus, the volumetric alpha blending for each pixel on the image can be expressed as:

$$c(x) = \sum_{i \in \mathcal{N}} c_i H\hat{G}_i(x) \prod_{j=1}^{i-1}\left(1 - H\hat{G}_j(x)\right) \tag{8}$$

where $\mathcal{N}$ is the sorted 3D Half-Gaussian set for the pixel and $H\hat{G}(x)$ is the integration of both halves of a 3D Half-Gaussian pair:

$$H\hat{G}(x) = \frac{1}{2}\left\{(\alpha_1 + \alpha_2) + (\alpha_1 - \alpha_2)\,\mathrm{erf}\left(\frac{n_1 x + n_2 y}{\sqrt{2}n_3}\right)\right\}\hat{G}_{\hat{\mathbf{\Sigma}}}(\hat{\mathbf{x}} - \hat{\mu}) \tag{9}$$

4　Experiments

4.1　Experimental Setup

Datasets and Metrics.

Following the published literature, we tested our design on 11 (indoor and outdoor) scenes from various datasets: 7 scenes from Mip-nerf360 dataset[1], 2 scenes from Tanks &Temples [9], and 2 scenes from DeepBlending [6]. Figure 4 shows sample images from these datasets. Consistent with prior studies, we use PSNR, SSIM [21] and LPIPS [28] to measure the performance on each dataset. We provide the averaged metrics over all scenes for each dataset in the main paper and put the full quantitative results for each scene in the Appendix.

Baselines and Implementation. To evaluate the general improvement brought by using a Half-Gaussian kernel in neural rendering, we ran experiments based on two baseline methods: vanilla-3D-GS and one of its extensions Scaffold-GS, where we replaced the reconstruction kernel with the Half-Gaussian kernel. We denote our models as 3D-HGS, and Scaffold-HGS, respectively. We compared performance against state-of-the-art 3D reconstruction methods: 3D-GS [8], Mip-NeRF [1], 2D-GS [7], Fre-GS [27], Scaffold-GS [13], and GES [5].

MipNeRF-360

Deep Blending   Tanks & Temples

Figure 4: **Training Images from MipNeRF-360, Deep Blending, and Tanks & Temples Datasets.**

For the implementation of 3D-HGS, we utilize the three (unused) normal parameters in 3D-GS to represent the normal vector of the splitting plane. Additionally, we learn two opacities for each Gaussian, corresponding to two halves. This results in only one additional parameter for each reconstruction kernel compared to the 3D-GS. The forward and backward passes of the rasterizer are modified based on the vanilla 3D-GS and Eq. 9. We adhered to the training settings and hyperparameters used in [8], setting the learning rate for the normal vector at 0.3 for the Deep Blending dataset and 0.003 for the other datasets. For the implementation of Scaffold-HGS, we did not increase the number of parameters in each Gaussian. Following the referenced paper, we employed an MLP to learn the normal vector based on the feature vector of each voxel and doubled the width of the output layer of the opacity MLP to accommodate two opacity values. The rasterizer was also modified based on Eq. 9. All other training settings were consistent with those described in [13]. All experiments were conducted on a machine equipped with an NVIDIA RTX 3090 GPU.

4.2 Results Analysis

Table 1: **Quantitative comparison to the SOTA methods on real-world datasets.** Competing metrics are extracted from respective papers.

Dataset	Mip-NeRF360			Tanks&Temples			Deep Blending		
Method	PSNR ↑	SSIM↑	LPIPS↓	PSNR↑	SSIM↑	LPIPS↓	PSNR↑	SSIM↑	LPIPS↓
3D-GS [8]	28.69	0.870	0.182	23.14	0.841	0.183	29.41	0.903	0.243
Mip-NeRF [1]	29.23	0.844	0.207	22.22	0.759	0.257	29.40	0.901	0.245
2D-GS[7]	28.98	0.867	0.185	23.43	0.845	0.181	29.70	0.902	0.250
Fre-GS [27]	27.85	0.826	0.209	23.96	0.841	0.183	29.93	0.904	0.240
Scaffold-GS [13]	28.84	0.848	0.220	23.96	0.853	0.177	30.21	0.906	0.254
GES [5]	28.69	0.857	0.206	23.35	0.836	0.198	29.68	0.901	0.252
3D-HGS (**Ours**)	29.56	0.873	0.178	24.49	0.857	0.169	29.76	0.905	0.242
Scaffold-HGS(**Ours**)	29.25	0.867	0.186	24.42	0.859	0.162	30.36	0.910	0.240

The quantitative results are presented in Tab. 1 and the Appendix. Plugging in the proposed Half Gaussian kernel, 3D-HGS and Scaffold-HGS, achieved state-of-the-art performance on the tested datasets. Both 3D-HGS and Scaffold-HGS outperformed their respective baselines, demonstrating a general improvement by using the 3D Half-Gaussian as the reconstruction kernel. Specifically, 3D-HGS achieved new SOTA PSNR performance on the MipNeRF360 and Tanks&Temples datasets and comparable results on the Deep Blending dataset. 3D-HGS outperformed 3D-GS on three datasets by 0.87, 1.35, and 0.35 PSNR, respectively. Additionally, 3D-HGS surpassed all previous methods on the Mip-NeRF360 and Tanks & Temples datasets in terms of SSIM and LPIPS, and achieved the second-best results on the DeepBlending dataset for SSIM and LPIPS. The 3D-HGS can learn better 3D scene representations of edges and texture-rich areas; however, the improvement is less pronounced on datasets with more feature-less areas (see Fig. 4). We also observed improvements by applying the 3D Half-Gaussian to Scaffold-GS, with Scaffold-HGS achieving new SOTA on the Deep Blending dataset.

Qualitative results are shown in Fig. 1. We observed that our method delivers better performance on fine-scale details (e.g., T&T-Truck, Mip360-Garden, Mip360-Bonsai, Mip360-Room), high-frequency
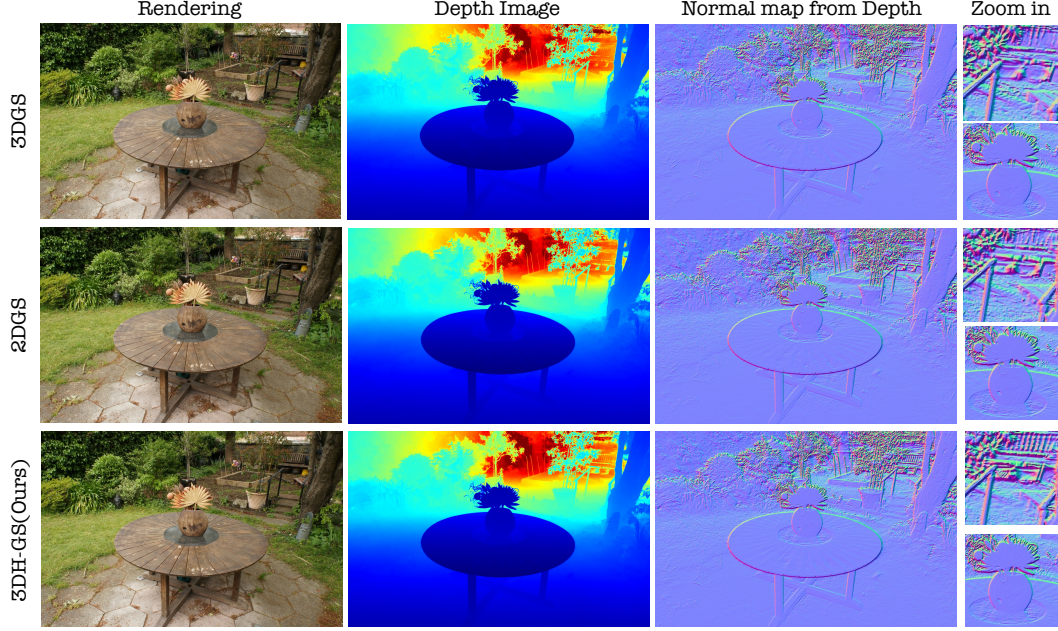
Figure 5: Comparison of Depth Images and Normal Maps. We visualize the depth maps alongside normals estimated from these maps. Our method demonstrates superior performance, capturing finer details in the bench structure and the surface textures of pots.

textures (e.g., T&T-Train, Mip360-Counter, Mip360-Bicycle), light rendering (e.g., Mip360-Garden, DB-DrJohnson), and shadow areas (e.g., T&T-Train, Mip360-Bonsai, DB-DrJohnson).

We also present the generated depth image and the corresponding estimated surface normal in Fig. 5. These depth images and normal maps were produced using the method described in [7]. Our results demonstrate that the proposed method is capable of generating accurate depth images, particularly excelling in capturing fine-grained surface textures.

4.3 Ablation Study

Different Reconstruction Kernels. We begin the ablation study by comparing the rendering performance of the four reconstruction kernels listed in Tab. 2.

Table 2: **Different reconstruction kernels**

3D Gaussian	$exp\{-\frac{1}{2}(\boldsymbol{x}-\boldsymbol{\mu})^T\boldsymbol{\Sigma}^{-1}(\boldsymbol{x}-\boldsymbol{\mu})\}$	2D Gaussian	$exp\{-\frac{1}{2}(\hat{\boldsymbol{x}}-\hat{\boldsymbol{\mu}})^T\hat{\boldsymbol{\Sigma}}^{-1}(\hat{\boldsymbol{x}}-\hat{\boldsymbol{\mu}})\}$
Generalized Exponential	$exp\{(-\frac{1}{2}(\boldsymbol{x}-\boldsymbol{\mu})^T\boldsymbol{\Sigma}^{-1}(\boldsymbol{x}-\boldsymbol{\mu}))^{\frac{\beta}{2}}\}$	3D Half-Gaussian	$u(\mathbf{n}^T\mathbf{x})\cdot exp\{-\frac{1}{2}(\boldsymbol{x}-\boldsymbol{\mu})^T\boldsymbol{\Sigma}^{-1}(\boldsymbol{x}-\boldsymbol{\mu})\}$

The 2D Gaussian kernel and generalized exponential kernels were proposed in [7] and [5], respectively. For a fair comparison, we used the same loss function and training iterations as the original 3D-GS. For details on the implementation of different kernels, please refer to the Appendix.

We present the PSNR score for each 3D scene, the average score for each dataset, and the total average score. The results are shown in Tab. 3. We used 3D-GS as the baseline, indicating improved results in red and decreased results in blue. Compared to the original 3D Gaussian kernel, the 3D Half-Gaussian kernel shows consistent improvement across all 3D scenes. While other kernels demonstrate superiority in some 3D scenes, they exhibit drawbacks in others. Overall, we achieved the best average performance across all 3D scenes.

Learning rate of normal. Since the normal of the splitting plane of the Half-Gaussian is a new parameter, we conducted an ablation study on the learning rate of this normal. Fig. 6 shows the PSNR scores and the means of the opacity differences between Half-Gaussian halves for the Tanks&Temples dataset at various learning rates. The means of the opacity differences indicate the degree of disparity between the two halves: higher values signify more distinct 3D Half-Gaussian halves. A low

Table 3: **PSNR scores ↑ of the rendering performance with different reconstruction kernels.**

Kernels	Tanks&Temples			Deep Blending			Mip-NeRF360								AVG
	Truck	Train	Avg	Playroom	Drjohnson	Avg	Bicycle	Garden	Kitchen	Stump	Room	Counter	Bonsai	Avg	
3D-GS	25.18	21.09	23.14	30.04	28.77	29.41	25.25	27.41	30.32	26.55	30.63	28.70	31.98	28.69	27.81
2D-GS	25.14	21.70	23.42	30.18	29.12	29.65	25.02	27.14	31.33	26.57	31.37	28.97	32.33	28.94	28.06
GES	24.94	21.73	23.34	30.29	29.35	29.82	24.87	27.07	31.07	26.17	31.17	28.75	31.97	28.72	27.94
3D-HGS	26.04	22.95	24.49	30.20	29.32	29.76	25.39	27.68	32.17	26.64	32.12	29.62	33.30	29.56	28.38

learning rate results in slow convergence of the normal, yielding results closer to the original 3D-GS. Conversely, a high learning rate leads to an unstable training process. For efficiency, we encourage greater disparity between the two Half-Gaussian halves. Based on our findings, we set the default learning rate to 0.003 for our experiments.
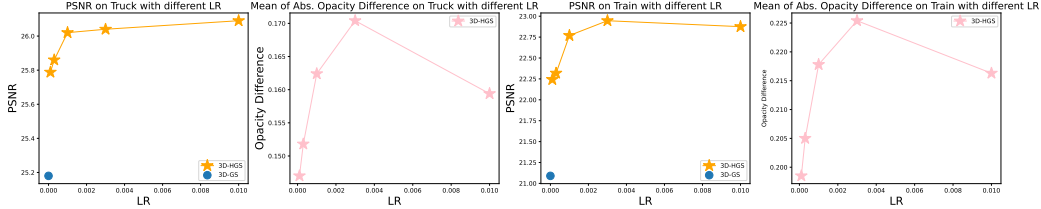

Figure 6: PSNR scores and the means of the opacities differences between Half-Gaussian halves with different normal learning rates. The means of the absolute opacity difference represents the disparity of half-gaussian halves.

Training strategy. Since 3D-HGS only introduces four new parameters compared to 3D-GS—normals and an additional opacity—and inspired by parameter-efficient fine-tuning (PEFT) [**?**], we compare four different training strategies: load a pre-trained 3D-GS into 3D-HGS and fine-tune all parameters without adaptive density control; fine-tune all parameters with adaptive density control; fine-tune only the normal and opacities; and train 3D-HGS from scratch. As shown in Tab. 4, training from scratch achieved the best results.

Table 4: **Ablation study for different training strategies.** Finetuning all starts from the pretrained 3D-GS model. Results are shown in the PSNR score.

Dataset	Iterations	Training strategies	3D-GS	Finetune	Finetune w/. density control	Selective Finetune	3D-HGS
Truck	30K	From scratch	25.18	/	/	/	**26.04**
	1K	Finetune	/	25.40	25.16	25.45	/
	5K	Finetune	/	25.54	25.36	25.48	/
	15K	Finetune	/	25.61	25.54	25.52	/
Train	30K	From scratch	21.09	/	/	/	**22.95**
	1K	Finetune	/	22.17	21.54	22.23	/
	5K	Finetune	/	22.19	21.65	22.15	/
	15K	Finetune	/	22.37	22.01	22.26	/

5   Limitations, Impact, and Conclusion

We proposed half-Gaussian splatting, a novel plug-and-play method for accurate 3D scene reconstruction. We propose to split each Gaussian into two half Gaussians and assign different opacities to each of them. Through this approach, we successfully achieve state-of-the-art results without compromising inference time. Furthermore, almost all architectures based on Gaussian splatting can easily adapt their kernel to half-Gaussian and benefit from the improvement without altering the structure of their network. Given that changing the kernel can impact performance, we also compared it against other kernel-changing methods. The results of these comparisons demonstrate that half-Gaussian splatting is a favorable kernel choice for 3D splatting methods.

Although 3D-HGS demonstrates remarkable results in novel scene generation, it still encounters challenges with geometry reconstruction in featureless areas. The excellent performance of 3D novel view synthesis could potentially lead to disinformation or the creation of fake profiles. Additionally, enhanced 3D reconstruction capabilities could result in increased surveillance and privacy violations, as more detailed models can be created without consent. It is crucial to ensure that the development and application of this technology prioritize security and privacy, minimizing any negative social impact.

References

[1] Jonathan T Barron, Ben Mildenhall, Matthew Tancik, Peter Hedman, Ricardo Martin-Brualla, and Pratul P Srinivasan. Mip-nerf: A multiscale representation for anti-aliasing neural radiance fields. In *Proceedings of the IEEE/CVF International Conference on Computer Vision*, pages 5855–5864, 2021.

[2] Guikun Chen and Wenguan Wang. A survey on 3d gaussian splatting. *arXiv preprint arXiv:2401.03890*, 2024.

[3] Anurag Dalal, Daniel Hagen, Kjell G Robbersmyr, and Kristian Muri Knausgård. Gaussian splatting: 3d reconstruction and novel view synthesis, a review. *arXiv preprint arXiv:2405.03417*, 2024.

[4] Kyle Gao, Yina Gao, Hongjie He, Dening Lu, Linlin Xu, and Jonathan Li. Nerf: Neural radiance field in 3d vision, a comprehensive review. *arXiv preprint arXiv:2210.00379*, 2022.

[5] Abdullah Hamdi, Luke Melas-Kyriazi, Guocheng Qian, Jinjie Mai, Ruoshi Liu, Carl Vondrick, Bernard Ghanem, and Andrea Vedaldi. Ges: Generalized exponential splatting for efficient radiance field rendering. *arXiv preprint arXiv:2402.10128*, 2024.

[6] Peter Hedman, Julien Philip, True Price, Jan-Michael Frahm, George Drettakis, and Gabriel Brostow. Deep blending for free-viewpoint image-based rendering. *ACM Transactions on Graphics (ToG)*, 37(6):1–15, 2018.

[7] Binbin Huang, Zehao Yu, Anpei Chen, Andreas Geiger, and Shenghua Gao. 2d gaussian splatting for geometrically accurate radiance fields. *arXiv preprint arXiv:2403.17888*, 2024.

[8] Bernhard Kerbl, Georgios Kopanas, Thomas Leimkühler, and George Drettakis. 3d gaussian splatting for real-time radiance field rendering. *ACM Transactions on Graphics*, 42(4):1–14, 2023.

[9] Arno Knapitsch, Jaesik Park, Qian-Yi Zhou, and Vladlen Koltun. Tanks and temples: Benchmarking large-scale scene reconstruction. *ACM Transactions on Graphics (ToG)*, 36(4):1–13, 2017.

[10] Zhe Li, Zerong Zheng, Lizhen Wang, and Yebin Liu. Animatable gaussians: Learning pose-dependent gaussian maps for high-fidelity human avatar modeling. *arXiv preprint arXiv:2311.16096*, 2023.

[11] Zhihao Liang, Qi Zhang, Wenbo Hu, Ying Feng, Lei Zhu, and Kui Jia. Analytic-splatting: Anti-aliased 3d gaussian splatting via analytic integration. *arXiv preprint arXiv:2403.11056*, 2024.

[12] Jiaqi Lin, Zhihao Li, Xiao Tang, Jianzhuang Liu, Shiyong Liu, Jiayue Liu, Yangdi Lu, Xiaofei Wu, Songcen Xu, Youliang Yan, et al. Vastgaussian: Vast 3d gaussians for large scene reconstruction. *arXiv preprint arXiv:2402.17427*, 2024.

[13] Tao Lu, Mulin Yu, Linning Xu, Yuanbo Xiangli, Limin Wang, Dahua Lin, and Bo Dai. Scaffold-gs: Structured 3d gaussians for view-adaptive rendering. *arXiv preprint arXiv:2312.00109*, 2023.

[14] Ricardo Martin-Brualla, Noha Radwan, Mehdi SM Sajjadi, Jonathan T Barron, Alexey Dosovitskiy, and Daniel Duckworth. Nerf in the wild: Neural radiance fields for unconstrained photo collections. In *Proceedings of the IEEE/CVF Conference on Computer Vision and Pattern Recognition*, pages 7210–7219, 2021.

[15] Ben Mildenhall, Pratul P Srinivasan, Matthew Tancik, Jonathan T Barron, Ravi Ramamoorthi, and Ren Ng. Nerf: Representing scenes as neural radiance fields for view synthesis. *Communications of the ACM*, 65(1):99–106, 2021.

[16] Jiawei Ren, Liang Pan, Jiaxiang Tang, Chi Zhang, Ang Cao, Gang Zeng, and Ziwei Liu. Dreamgaussian4d: Generative 4d gaussian splatting. *arXiv preprint arXiv:2312.17142*, 2023.

[17] Johannes L Schonberger and Jan-Michael Frahm. Structure-from-motion revisited. In *Proceedings of the IEEE conference on computer vision and pattern recognition*, pages 4104–4113, 2016.

[18] Steven M Seitz, Brian Curless, James Diebel, Daniel Scharstein, and Richard Szeliski. A comparison and evaluation of multi-view stereo reconstruction algorithms. In *2006 IEEE computer society conference on computer vision and pattern recognition (CVPR'06)*, volume 1, pages 519–528. IEEE, 2006.

[19] Xiaowei Song, Jv Zheng, Shiran Yuan, Huan-ang Gao, Jingwei Zhao, Xiang He, Weihao Gu, and Hao Zhao. Sa-gs: Scale-adaptive gaussian splatting for training-free anti-aliasing. *arXiv preprint arXiv:2403.19615*, 2024.

[20] Haithem Turki, Deva Ramanan, and Mahadev Satyanarayanan. Mega-nerf: Scalable construction of large-scale nerfs for virtual fly-throughs. In *Proceedings of the IEEE/CVF Conference on Computer Vision and Pattern Recognition*, pages 12922–12931, 2022.

[21] Zhou Wang, Alan C Bovik, Hamid R Sheikh, and Eero P Simoncelli. Image quality assessment: from error visibility to structural similarity. *IEEE transactions on image processing*, 13(4):600–612, 2004.

[22] Lee Westover. Interactive volume rendering. In *Proceedings of the 1989 Chapel Hill workshop on Volume visualization*, pages 9–16, 1989.

[23] Lee Westover. Footprint evaluation for volume rendering. In *Proceedings of the 17th annual conference on Computer graphics and interactive techniques*, pages 367–376, 1990.

[24] Tong Wu, Yu-Jie Yuan, Ling-Xiao Zhang, Jie Yang, Yan-Pei Cao, Ling-Qi Yan, and Lin Gao. Recent advances in 3d gaussian splatting. *arXiv preprint arXiv:2403.11134*, 2024.

[25] Yunzhi Yan, Haotong Lin, Chenxu Zhou, Weijie Wang, Haiyang Sun, Kun Zhan, Xianpeng Lang, Xiaowei Zhou, and Sida Peng. Street gaussians for modeling dynamic urban scenes. *arXiv preprint arXiv:2401.01339*, 2024.

[26] Zehao Yu, Anpei Chen, Binbin Huang, Torsten Sattler, and Andreas Geiger. Mip-splatting: Alias-free 3d gaussian splatting. *arXiv preprint arXiv:2311.16493*, 2023.

[27] Jiahui Zhang, Fangneng Zhan, Muyu Xu, Shijian Lu, and Eric Xing. Fregs: 3d gaussian splatting with progressive frequency regularization. *arXiv preprint arXiv:2403.06908*, 2024.

[28] Richard Zhang, Phillip Isola, Alexei A Efros, Eli Shechtman, and Oliver Wang. The unreasonable effectiveness of deep features as a perceptual metric. In *Proceedings of the IEEE conference on computer vision and pattern recognition*, pages 586–595, 2018.

[29] Cheng Zhao, Su Sun, Ruoyu Wang, Yuliang Guo, Jun-Jun Wan, Zhou Huang, Xinyu Huang, Yingjie Victor Chen, and Liu Ren. Tclc-gs: Tightly coupled lidar-camera gaussian splatting for surrounding autonomous driving scenes. *arXiv preprint arXiv:2404.02410*, 2024.

[30] Matthias Zwicker, Hanspeter Pfister, Jeroen Van Baar, and Markus Gross. Ewa volume splatting. In *Proceedings Visualization, 2001. VIS'01.*, pages 29–538. IEEE, 2001.

[31] Matthias Zwicker, Hanspeter Pfister, Jeroen Van Baar, and Markus Gross. Surface splatting. In *Proceedings of the 28th annual conference on Computer graphics and interactive techniques*, pages 371–378, 2001.

[32] Matthias Zwicker, Hanspeter Pfister, Jeroen Van Baar, and Markus Gross. Ewa splatting. *IEEE Transactions on Visualization and Computer Graphics*, 8(3):223–238, 2002.

A Appendix

A.1 Implementation details

Implementation of 3D-HGS We implemented our method in Python using the PyTorch framework and modified custom CUDA kernels for rasterization. We run $30k$ iterations to train, and before $20k$ iterations we will prune and grow points every 100 iterations, the opacity reset step will be applied after 3000 iterations and stop at $20k$ iterations. We followed 3D-GS to set up all other parameters in our architecture. We use the same loss function from 3D-GS:

$$\mathcal{L} = (1 - \lambda)\mathcal{L}_1 + \lambda\mathcal{L}_{SSIM} \tag{10}$$

We also use $\lambda = 0.2$ in our implementation.

Implementation of Scaffold-HGS Like Scaffold-GS, we use 2 layer MLPs to get the normals for each kernel. We follow the original paper to use offset $k = 10$, and length of hidden features 32. An anchor is pruned if the accumulated opacity (each offset has two opacities) of its neural Gaussians is less than 0.5 at each round of refinement. We also used the same training loss as Scaffold-GS:

$$\mathcal{L} = \mathcal{L}_1 + \lambda_{SSIM}\mathcal{L}_{SSIM} + \lambda_{vol}\mathcal{L}_{vol} \tag{11}$$

The λ_{SSIM} is set to 0.2 and λ_{vol} is set to 0.001. We train the model for $30k$ iterations.

Hardware. We run all the experiments on a machine with a single NVIDIA RTX 3090 GPU, and AMD EPYC 7302 CPU.

Implementation of different kernel experiment. We describe the experiment set up for Tab. 3. We use the loss function from the original 3D-GS, as in Eq. 10. We train all the methods for $30k$ iterations, and we also perform adaptive density control for the first $15k$ iterations. The implementation of the 2D Gaussian kernel is from [7], and the generalized exponential kernel is from [5].

A.2 More results

Here we show detailed quantitative results of Tab. 1 on each scene.

Table 5: **Quantitative comparison to previous methods Tanks&temples and Deep blending we choose dataset.** Competing metrics are extracted from respective papers.

	Tanks&Temples						Deep Blending					
Dataset	Truck			Train			Playroom			Drjohnson		
Method	PSNR ↑	SSIM↑	LPIPS↓	PSNR↑	SSIM↑	LPIPS↓	PSNR↑	SSIM↑	LPIPS↓	PSNR↑	SSIM↑	LPIPS↓
3D-GS [8]	25.18	0.879	0.148	21.09	0.802	0.218	30.04	0.906	0.241	28.77	0.899	0.244
Mip-NeRF [1]	24.91	0.857	0.159	19.52	0.66	0.354	29.66	0.900	0.252	29.14	0.901	0.237
Scaffold-GS [13]	25.77	0.883	0.147	22.15	0.822	0.206	30.62	0.904	0.258	29.80	0.907	0.250
3D-HGS (Ours)	26.04	0.887	0.141	22.95	0.827	0.197	30.20	0.907	0.243	29.32	0.904	0.240
Scaffold-HGS(Ours)	26.03	0.886	0.134	22.80	0.832	0.190	30.90	0.911	0.243	29.82	0.908	0.238

Table 6: **Quantitative comparison to previous methods on Mip-nerf360 dataset** Competing metrics are extracted from respective papers.

Metrics	PSNR ↑	SSIM↑	LPIPS↓	PSNR↑	SSIM↑	LPIPS↓	PSNR↑	SSIM↑	LPIPS↓	PSNR↑	SSIM↑	LPIPS↓
3D Scenes	Stump			Room			Counter			bonsai		
3D-GS [8]	26.55	0.775	0.210	30.63	0.914	0.220	28.70	0.905	0.204	31.98	0.938	0.205
Mip-NeRF [1]	26.40	0.744	0.261	31.63	0.913	0.211	29.55	0.894	0.204	33.46	0.941	0.176
Scaffold-GS [13]	26.27	0.784	0.284	31.93	0.925	0.202	29.34	0.914	0.191	32.70	0.946	0.185
3D-HGS (Ours)	26.64	0.770	0.215	32.12	0.921	0.220	29.62	0.909	0.201	33.30	0.950	0.180
Scaffold-HGS(Ours)	26.45	0.758	0.239	32.06	0.921	0.213	29.40	0.906	0.207	32.71	0.947	0.180
3D Scenes	Bicycle			Garden			Kitchen					
3D-GS [8]	25.25	0.771	0.205	27.41	0.868	0.103	30.32	0.922	0.129			
Mip-NeRF [1]	24.37	0.685	0.301	26.98	0.813	0.170	32.23	0.920	0.127			
Scaffold-GS [13]	24.50	0.705	0.306	27.17	0.842	0.146	31.30	0.928	0.126			
3D-HGS (Ours)	25.39	0.768	0.202	27.68	0.868	0.104	32.17	0.930	0.125			
Scaffold-HGS(Ours)	25.20	0.757	0.226	27.40	0.860	0.115	31.56	0.926	0.127			